Prepared for Medical Engineering & Physics
Submitted on September 18, 2013
Revised on February 20, 2014
Final submission on April 17, 2014

A Viscoelastic Poromechanical Model of the Knee Joint in Large Compression

M. Kazemi and L.P. Li *

Department of Mechanical and Manufacturing Engineering, University of Calgary,
2500 University Drive, N.W., Calgary, Alberta, Canada T2N 1N4

*Corresponding author:
LePing Li, Ph.D., P.Eng., Associate Professor
Department of Mechanical and Manufacturing Engineering
University of Calgary
2500 University Drive, N.W.
Calgary, Alberta, Canada T2N 1N4

Phone: 1 403 210 7537; Fax: 1 403 282 8406
Email: Leping.Li@ucalgary.ca

Abstract

The elastic response of the knee joint in various loading and pathological conditions has been investigated using anatomically accurate geometry. However, it is still challenging to predict the poromechanical response of the knee in realistic loading conditions. In the present study, a viscoelastic, poromechanical model of the knee joint was developed for soft tissues undergoing large deformation. Cartilages and menisci were modeled as fibril-reinforced porous materials and ligaments were considered as fibril-reinforced hyperelastic solids. Quasi-linear viscoelasticty was formulated for the collagen network of these tissues and nearly incompressible Neo-Hookean hyperelasticity was used for the non-fibrillar matrix. The constitutive model was coded with a user defined FORTRAN subroutine, in order to use ABAQUS for the finite element analysis. Creep and stress relaxation were investigated with large compression of the knee in full extension. The contact pressure distributions were found similar in creep and stress relaxation. However, the load transfer in the joint was completely different in these two loading scenarios. During creep, the contact pressure between cartilages decreased but the pressure between cartilage and meniscus increased with time. This led to a gradual transfer of some loading from the central part of cartilages to menisci. During stress relaxation, however, both contact pressures decreased monotonically.

Keywords**:** Fluid pressure; Creep; Stress relaxation; Finite deformation; Human knee joint; Finite element analysis

1. Introduction

The elastic response of the knee joint in different loading and pathological conditions has been extensively investigated using three-dimensional (3D) finite element (FE) models. For instance, the contact mechanics of the healthy and meniscectomized knee joints were investigated under large compression [1]. The in-situ ligament forces and joint kinematics were validated against experimental data [2]. The effects of boundary conditions and bone deformation on contact stresses were clarified [3]. The role of collagen fibrils of articular cartilage in the mechanical function of the knee was studied [4]. Total and partial meniscectomies have been also investigated using 3D computational models [5-9]. Cartilage injury and osteochondral defects have been investigated by several research groups [10-12].

In all these studies, cartilages and menisci were modeled as elastic, i.e. the fluid flow and the relevant time-dependent behavior were not considered. It was believed that these models could be used to approximate the instantaneous load response of the joint, when the fluid is trapped in the tissues. In fact, the instantaneous behavior of fluid-saturated materials is elastic [13,14]. Therefore, a Poisson's ratio of 0.45-0.48 and a large effective elastic modulus have often been used in elastic modeling to approximate the incompressible response of the tissues at fast knee compression.

Fluid pressurization has been implemented in axisymmetric or 2D modeling of the knee joint [15-17]. Moreover, a finite sliding, frictionless contact model of porous media was developed to study the contact of 3D cartilage layers in finite deformations [18]. In anatomically accurate modeling of human joints, one of the first 3D poromechanical models was developed to study the internal derangement of the temporomandibular joint [19]. An anatomically accurate 3D knee joint model was developed to account for the fluid pressurization and fibril-reinforcement in

cartilages and menisci [20]. The fibril-reinforced poromechanical model was compared to a single-phase elastic model of the knee, and different predictions were obtained for the instantaneous response [21]. The creep behavior of the intact and meniscectomized knee joints was also investigated [22, 23]. In all these poromechanical studies of the knee joint, however, the small deformation theory was used to accelerate numerical convergence. Only the short-term load response of the knee with soft tissues in large deformation was investigated using a fibril-reinforced model of articular cartilages and an elastic model of menisci [24, 25].

A finite deformation theory needs to be incorporated in the knee joint modeling, in order to predict the viscoelastic poromechanical response in physiological conditions. In the present study, large deformations were formulated in a nonlinear, fibril-reinforced poromechanical model for cartilages and menisci. The creep and stress relaxation of the knee joint in full extension was investigated and the results were compared to the experimental data from the literature.

2. Methods

Cartilages and menisci were modeled as fully saturated porous media reinforced with a continuum collagen network. Ligaments were considered as fibril-reinforced solid materials because fluid pressurization is not significant in tension. Nearly incompressible, Neo-Hookean hyperelasticity was considered for the non-fibrillar solid matrix of tissues. Quasi-linear viscoelasticty [26, 27] was employed for the collagen network. The numerical formulation of the constitutive model was performed in a co-rotational reference frame to preserve objectivity (i.e. frame indifference) of stress rates. A user defined FORTRAN subroutine, UMAT, was coded for the numerical implementation. The UMAT was then numerically verified and experimentally validated using simple geometries prior to the use in the joint modeling

2.1 *Formulation of the Non-fibrillar Matrix*

Denoting the current coordinate of a material point by $\mathbf{x}$ and its reference coordinate by $\mathbf{X}$, the deformation gradient $\mathbf{F}$, the total volume change at the point, J, and the distortional component of deformation gradient, $\overline{\mathbf{F}}$, can be defined, respectively, as [28]

$$\mathbf{F} = \frac{\partial \mathbf{x}}{\partial \mathbf{X}}, \quad J = \det(\mathbf{F}), \quad \overline{\mathbf{F}} = J^{-1/3}\mathbf{F} \tag{1}$$

The right Cauchy-Green deformation tensor, $\mathbf{C}$, its distortional component, $\overline{\mathbf{C}}$, and the first invariant of $\overline{\mathbf{C}}$, $\bar{I}_1$, can now be found as

$$\mathbf{C} = \mathbf{F}^T\mathbf{F}, \quad \overline{\mathbf{C}} = \overline{\mathbf{F}}^T\overline{\mathbf{F}}, \quad \bar{I}_1 = tr\left(\overline{\mathbf{C}}\right) = \overline{\mathbf{C}} : \mathbf{I} \tag{2}$$

in which $\mathbf{I}$ is the identity tensor.

The strain energy function for a nearly incompressible, Neo-Hookean material can be introduced as

$$W(\bar{I}_1, J) = C_{10}(\bar{I}_1 - 3) + \frac{1}{D_1}(J-1)^2 \tag{3}$$

where C_{10} and D_1 are measures of shear modulus and bulk modulus, respectively. The Cauchy stress tensor in the non-fibrillar matrix, $\boldsymbol{\sigma}^m$, is obtained from the push forward of the second Piola-Kirchhoff stress in the matrix, $\mathbf{S}^m$

$$\boldsymbol{\sigma}^m = J^{-1}\mathbf{F}\mathbf{S}^m\mathbf{F}^T \qquad \text{where} \quad \mathbf{S}^m = 2\frac{\partial W}{\partial \mathbf{C}} \tag{4}$$

The Cauchy stress takes the indicial form

$$\sigma_{ij}^m = \frac{2}{J}C_{10}\left(\overline{B}_{ij} - \frac{1}{3}\overline{B}_{kk}\delta_{ij}\right) + \frac{2}{D_1}(J-1)\delta_{ij} \tag{5}$$

in which $\overline{\mathbf{B}} = \overline{\mathbf{F}}\overline{\mathbf{F}}^T$ is the distortional left Cauchy-Green deformation tensor.

For large deformations and geometric nonlinearities, the material Jacobian tensor needs to be obtained from an objective stress rate. The Jaumann rate is commonly used in FE implementations and is used in ABAQUS for continuum elements. The Kirchhoff stress and its Jaumann rate can be obtained as

$$\boldsymbol{\tau}^m = J\boldsymbol{\sigma}^m, \quad \overset{\nabla}{\boldsymbol{\tau}}^m = \dot{\boldsymbol{\tau}}^m - \mathbf{W}\boldsymbol{\tau}^m + \boldsymbol{\tau}^m\mathbf{W} \tag{6}$$

where $\boldsymbol{\tau}^m$ is the Kirchhoff stress and $\dot{\boldsymbol{\tau}}^m$ is Kirchhoff stress rate, $\overset{\nabla}{\boldsymbol{\tau}}^m$ is its Jaumann rate, and $\mathbf{W}$ is the spin tensor. The material Jacobian of the non-fibrillar matrix, $\mathbf{D}^m$, can now be found from variation in the Jaumann rate of the Kirchhoff stress (ABAQUS Manual, 2011)

$$\delta\overset{\nabla}{\boldsymbol{\tau}}^m = J\mathbf{D}^m : \delta\mathbf{d} \tag{7}$$

where $\mathbf{d}$ is the rate of deformation tensor. The components of the fourth order tensor, D^m_{ijkl}, can be found as (ABAQUS Manual, 2011)

$$D^m_{ijkl} = \frac{2}{J}C_{10}\left(\frac{1}{2}\left(\delta_{ik}\overline{B}_{jl} + \overline{B}_{ik}\delta_{jl} + \delta_{il}\overline{B}_{jk} + \overline{B}_{il}\delta_{jk}\right) - \frac{2}{3}\delta_{ij}\overline{B}_{kl} - \frac{2}{3}\overline{B}_{ij}\delta_{kl} + \frac{2}{9}\delta_{ij}\delta_{kl}\overline{B}_{mm}\right) + \frac{2}{D_1}(2J-1)\delta_{ij}\delta_{kl} \tag{8}$$

2.2 *Stresses and Material Jacobian of the Fibrillar Network*

At each material point, the fibrillar properties were defined in three local coordinate directions, *x, y* and *z*. This enables defining an anisotropic behavior, when the local coordinate system at different points is oriented in different directions. It was assumed that fibers only resist tension. Therefore, zero stiffness was assigned for fibers in compression. Furthermore, shearing was born by the non-fibrillar matrix only. For the fibers aligned in the *x* direction and subjected to tensile

strain in the x direction, the Cauchy stress in the fibrillar matrix based on the quasi-linear viscoelasticity (QLV) can be expressed as [27]

$$\sigma_x^f(t) = \int_0^t G_x(t-\tau)\frac{\partial \sigma_x^e}{\partial \varepsilon_x}\frac{\partial \varepsilon_x}{\partial \tau}d\tau \tag{9}$$

where σ_x^f is the stress in the fibrillar network, rather than the stress in an individual fiber. G_x is called reduced relaxation function, σ_x^e is the elastic stress in the fibrillar matrix and ε_x is the logarithmic strain. These variables are all for the x direction. The same equation, but with subscripts y or z, can be derived for the y or z direction, respectively. The reduced relaxation function is often expressed in terms of exponentials

$$G_x(t) = 1 + \sum_m g_x^m \exp(-t/\lambda_x^m) \tag{10}$$

where g_x^m are the weight constants and λ_x^m are the characteristic times for the viscoelastic dissipation.

The tensile elastic stress, σ_x^e, is based on the nonlinear stress-strain behavior of the tissues at equilibrium and is assumed as quadratic here [29]

$$\sigma_x^e(\varepsilon) = A_x\varepsilon_x + B_x\varepsilon_x^2 \tag{11}$$

where A_x and B_x are constants. This stress is set to zero if fibers are in compression in the x-direction. The viscoelastic stress (9) can then be numerically determined by (A-7), as shown in Appendix A. The Cauchy stress in the solid is the sum of the stresses in the non-fibrillar matrix and fibrillar network.

Now consider the numerical approximation of the material Jacobian for the fibrillar network, $\mathbf{D}^f$. We note that only the first integral of Eq. (A-1) depends on $\Delta\varepsilon_{k+1}$. Therefore, the material Jacobian can be approximated as:

$$D_{ii}^{f} = \frac{\partial \Delta \sigma_i^{f}(t+\Delta t)}{\partial \Delta \varepsilon_i (t+\Delta t)} = G_i(\Delta t) \times \left(A_i + 2B_i \varepsilon_i \right), \quad i = x, y, z$$
$$D_{ij}^{f} = 0, \quad i \neq j \tag{12}$$

In general, the material Jacobian is a fourth order tensor. However, in this case, it is assumed that the fibers only act in tension (zero stiffness in compression) and there is no shear interaction between the individual fibers. Therefore, the material Jacobian $\mathbf{D}^{f}$ is shown in the form of a second order tensor. In order to form the material Jacobian for the tissue, D_{xx}^{f}, D_{yy}^{f} and D_{zz}^{f} must be added to the first three diagonal elements of the Jacobian for the non-fibrillar matrix, D_{xxxx}^{m}, D_{yyyy}^{m} and D_{zzzz}^{m} in Eq. (8).

2.3 *Verification and Validation of the User-defined Material Model, UMAT*

The convergence of UMAT was verified using single and multiple elements in different loading and boundary conditions (known as patch test). Porous and solid elements with and without fibril-reinforcement were examined to ensure correct update of material Jacobian and stress tensor.

Stress relaxation and creep data [30] were used to validate the material model. The experiments were performed on 8 bovine cartilage explants with 3.08±0.08 mm in diameter and 1.61±0.08 mm in thickness. Both creep and stress relaxation tests were performed continuously on each specimen. A 3-step ramp compression and relaxation was applied: in each step, a displacement of 22 μm was applied at 2.0 μm/s followed by 1200 s relaxation. Similarly, a 3-step creep loading was used: in each step, a compressive force of 8 g was applied in 1.6 seconds, followed by 4000 s creep [30].

One best fit is presented here (Fig. 1). The material properties were summarized in Table 1. For the anisotropic fibrillar network, 24 material parameters were required, if the reduced relaxation function was approximated by 3 terms (2 in Eq. (11) and 6 in Eq. (10), times 3 directions). To avoid complexities in the data fit, the fibrillar properties were considered identical in the three directions. Therefore, the fibrillar properties were reduced to 8 (Table 1).

2.4 *Knee Geometry and Finite Element Mesh*

The geometry of the knee joint (Figure 2) was reconstructed from MRI data of a healthy male subject (27 years old, right knee). Cartilages and menisci were meshed using 20-node reduced integration hexahedral elements (C3D20RP). Ligaments were meshed using 8 node hexahedral elements (C3D8). Bones were assumed as rigid and their surfaces were discretized using triangular elements.

Structured mesh generation was performed with special care on elements' aspect ratios and minimizing the number of distorted elements. Four and three layers of elements were generated, respectively, for the femoral and tibial cartilages. Four layers of elements were also generated for each meniscus. The average aspect ratio of elements was 3.3 for cartilages and 3.4 for menisci. A total number of 28176 elements were used including 7476 for the femoral cartilage, 4638 for the tibial cartilages, 4144 for the menisci, 3593 for the ligaments and 8595 for the bones. The number of distorted elements was only 0.1% for the cartilages and 0.3% for the menisci (an angle $< 45^{o}$ or $> 135^{o}$).

A step-by-step mesh sensitivity analysis was conducted using further refined meshes (Table 2). Our strategy was to probe the mesh size effect on contact pressures. In the first step, the

femoral cartilage was refined with four times as many elements whereas other tissue meshes remained unchanged. Insignificant difference was found for the maximum contact pressure (Table 2). In the second step, the reference mesh of menisci was also replaced by a refined mesh. Finally, the reference mesh of all tissues was replaced by a refined mesh (Table 2). It was found that the contact distribution in each tissue was almost unchanged in all mesh refinements. Therefore, the original mesh was used for further results.

2.5 *Material Properties, Load and Boundary Conditions for the Joint Modeling*

Material properties of the tissues (Table 3) were chosen to be consistent with previous studies [4,22,29,31,32]. Three terms were taken for the reduced relaxation function (Eq. 10) [33,34]. The fibrillar network was considered orthotropic while the non-fibrillar matrix was considered isotropic. The hydraulic permeability was higher in the fiber direction [22,35].

The fiber orientation in the femoral cartilage (the x direction in Table 3) was determined based on the split-line patterns [36]. For the menisci, primary collagen fibers were oriented in the circumferential direction. Random fiber orientation was assumed for the tibial cartilages. The initial strains in the ligaments were chosen to be close to those from previous studies: 2.5% in ACL, 2% in MCL and LCL, and nil in PCL [1,37,38]. The initial strains were converted to initial stresses with reference to measurements [37] and applied as initial stress conditions.

Both creep and relaxation of the knee were considered. For creep, a compressive force of 700N was applied to the femur in proximal-distal direction; for relaxation, a knee compression of 0.6 mm was applied. The load/displacement was applied in 1s and held constant up to 200s. The femur was unconstrained in all translations but fixed in all rotations [39,40]. Tibia and fibula

were fixed at the bottom. Fluid exudation was permitted through the free surfaces of cartilaginous tissues. Moreover, fluid flow was allowed cross the contacting surfaces of cartilages and menisci using CONTACT PERMEABILITY option. Geometrical nonlinearities in large deformation were included using NLGEOM option in ABAQUS.

2.6 *Solution Techniques*

Finite sliding, surface to surface contact was modeled between femoral cartilage and menisci, femoral and tibial cartilages and menisci and tibial cartilages. Therefore, 6 contact pairs were defined, with 3 on the medial and 3 on the lateral sides. Frictional contact with coefficient of 0.02 [41] was considered for all contact surfaces. The penalty method was used to enforce the contact constraint. Implicit consolidation analysis in ABAQUS Standard was used for the FE simulations. Computations were performed using 12 parallel CPUs and up to 36 GB of RAM (Queen's University). A typical simulation of 200s was finished in about a week with almost two days to complete the analysis of the loading phase (i.e. the first second).

3. Results

For the creep case, the maximum contact pressure was in the medial side (Fig. 3). As creep developed, the contact area increased and the maximum contact pressure decreased (Fig. 3b vs. 3a). Although the contact pressure in the medial condyle decreased by 37% in 99s, the contact pressure in the lateral condyle decreased only by 5%. This resulted in more uniform contact pressure across the condyles in late creep (Fig. 3a vs. 3b). Moreover, as the maximum contact pressure decreased in the femoral cartilage, it increased in the menisci during early creep (Fig.

4a). However, the maximum contact pressures in both cartilage and meniscus decreased with relaxation (Fig. 4b).

The vertical displacement of the femur exhibited a nonlinear response and reached 0.65mm under 700N compressive force applied in 1s (Fig. 5). The maximum compressive strain prior to creep in the surface of tibial cartilages was about 0.31 in the medial and 0.20 in the lateral compartments (Fig. 6a). As creep developed, cartilage strain increased subsequently (Fig. 6b vs. 6a). The medial compartment was subjected to significantly higher strains in the loading phase as compared to the lateral compartment (Fig. 6a). The strains in the two compartments became closer as creep developed (Fig. 6b).

The maximum fluid pressure was found in the medial condyle prior to creep. Similar to contact pressure, the fluid pressure was more uniform across the condyles as creep developed (not shown). No considerable change in the fluid pressure was observed (Fig. 7) when the viscoelastic fibrillar stress (Eq. 9) was replaced by the elastic fibrillar stress (Eq. 11), provided that the elastic constants in Eq. (11) measured at equilibrium were replaced by the corresponding constants measured at the instantaneous response.

The maximum principal stress (tensile) was predominantly aligned in the fiber direction, i.e. in the directions of split lines for the femoral cartilage and in the circumferential direction for the meniscus (not shown). For the stress relaxation of 0.6 mm compression, the reaction force in the femur was about 600N. Maximum contact pressure was observed in the medial compartment and overall contact distribution was similar to that of creep (not shown).

4. Discussion

4.1 *Model Verification and Validation*

Verifications and validations were done at two levels, first for the constitutive model and its UMAT subroutine, second for the knee joint model. At the first level, numerical formulation and the UMAT were verified by the patch test for several scenarios. The constitutive model was validated against multistep creep and relaxation tests in unconfined compression (Fig. 1). Furthermore, the present constitutive model was parallel to the previous one with small deformation [32,34], which has been validated with various test data.

At the second level, the convergence of the knee model was somehow indicated in the step-by-step mesh sensitivity analysis (Table 2). The sensitivity analysis showed acceptable numerical precision when the reference mesh was used; it is not realistic presently to seek better numerical precisions for such complicated problems.

Measurements from the literature were used to partially validate our knee joint modeling. The predicted femoral axial displacement exhibited a nonlinear behavior and reached 0.65mm at 700N. This was in agreement with experimental data (Fig. 5). The maximum compressive strain in the surface of tibial cartilages was about 0.30 in the medial and 0.20 in the lateral compartments prior to creep (Fig. 6a). In in-vivo measurement, the peak cartilage deformation in full extension and under weight-bearing single-leg stance was 0.25±0.1 for the medial and 0.22±0.1 for the lateral compartments [43]. Considering that the 700N load used in our study was about the subject's body weight, our prediction seemed to be reasonable.

The predicted joint contact areas and contact pressures seemed to be reasonable too. Under 700N load prior to creep, the contact area in tibial plateau was 551 mm^2 for the medial and 581

mm^2 for the lateral sides, resulting in a total contact area of 1132 mm^2. These values were in the reported range in the literature: 960±170 [44] and 1125±180 mm^2 [45] under 500N force; 1150±200 [44], 1250±100 [45] and ~1039 mm^2 [46] under 1000N force. The predicted average contact pressure on the tibial plateau was 0.84 MPa on the medial and 0.6 MPa on the lateral compartments. The measured average contact pressures were 0.48 MPa under 445N [47], 0.82 MPa under 668N [48] and 1.1 MPa under 1000N [40]. Again, our prediction was in the reported range.

Consistent with the experimental studies [39,44], the maximum contact pressure occurred in the medial compartment (Fig. 3). However, the predicted contact pressure of 1.28 MPa was on the lower end of the reported range: 2.9 MPa at 500N [39], 1.33 MPa at 750N [49], 3.0 MPa [44] and 4.76 MPa [46] at 1000N. These differences could be resulted from the individual differences of the joints, as we see diverse data from the literature. However, the tissue properties used in the finite element simulations might be another source that caused this discrepancy.

4.2 *Creep vs Stress relaxation*

Fluid pressure dissipation was much slower in creep than in stress relaxation (Fig. 7), which was supported by the mechanical tests with explants [30]. This phenomenon is consistent with the physics of creep and stress relaxation. In stress relaxation, the applied displacement is held constant resulting in reduced reaction in the joint (not shown) with the fluid loss. The fluid pressure thus decreases with time. In creep, the fluid pressure dissipation is slowed down by increased deformation (Fig. 6a vs. 6b) that maintains the constant joint reaction: the fluid loss in the tissue reduces the fluid pressure, while increased tissue deformation raises the fluid pressure. In both cases, however, the fluid pressure supported a substantial portion of the loading for some time.

The contact pressure distribution was similar in creep and stress relaxation. The maximum contact pressure was in the medial compartment for both cases. The difference in contact pressures between the condyles diminished as creep or relaxation developed (Fig. 3 for creep). These similarities in creep and relaxation are reasonable as the joint contact is predominantly determined by the contact geometry. It is generally accepted that the medial compartment supports more loading at the instant of loading [39,44]. Our results support this point and yet provide more details about the time-dependent load transfer in the knee joint. The fluid pressurization likely provides more load support in the medial than lateral compartments. When the fluid pressure diminishes, more balanced load support occurs between the compartments.

The load transfer from cartilage to meniscus were fundamentally different in creep and stress relaxation. As creep continued, the contact pressure between cartilages decreased but the contact pressure between cartilages and menisci increased (Fig. 4a). Whereas in the relaxation case, both contact pressures decreased monotonically with time (Fig. 4b). This phenomenon seems to be logical since the total force in the joint is constant in creep: when the contact pressure decreases in the central area, it must increase in the periphery (note also the contact area increases a little with creep). During relaxation, the total force in the joint decreases with time, resulting in a general reduction of the contact pressure. It is worth mentioning that our creep results seemed to contradict the indentation test data in the literature [50] in which similar pressure patterns were obtained in cartilage-to-cartilage and indenter-to-cartilage measurements. The contrast was likely due to the difference in the contact conditions between the knee and the indentation setups. In the present study, the wedge-shape geometry of the menisci and their radial/circumferential motion facilitated time-dependent changes in the joint contact areas during creep. In the measurements [50], however, the disk-shape specimens would not allow changes in the contact areas.

4.3 *Collagen Viscoelasticity and Fiber Orientation*

Virtually the same fluid pressures were obtained (Fig. 7), when the reduced relaxation function was replaced by its initial value (i.e. use $G_x(0)$ in Eq. 9). The collagen stiffness reduction history described by the relaxation function had little effect on the fluid pressurization in the tissues. Therefore, it may not be always necessary to model collagen viscoelasticity, but the short-term fibrillar modulus must be used if the collagen network is considered elastic. The same finding has been reported in tissue explants modeling [34]. It must be noted that not all results will remain the same when the collagen viscoelasticity is ignored [34].

The maximum principal stress was essentially oriented in the direction of primary fibers (not shown). This result seems logical as fibers in the tissues are supposed to support the tensile stresses resulted from knee compression due to the Poisson's effect and fluid pressure.

4.4 *Fluid Pressurization in Menisci*

The result showed partial load transfer from cartilages to menisci during creep (Fig. 4a), which is consistent with the mechanical function of the menisci. This function of menisci cannot be fully understood without the present poromechanical modeling. Further results indicated that the load transfer was facilitated by the fluid pressure in the menisci. We performed additional simulations with menisci modeled as a transversely isotropic solid whereas cartilages were still modeled as a fibril-reinforced fluid-saturated material. The result showed a constant contact pressure (for 50s simulations) in cartilages and menisci during creep. This may suggest that the fluid in meniscus is essential to produce the observed creep response of the joint although further investigations are required to confirm this preliminary result.

The challenge in poromechanical modeling of the knee joint is more or less related to the double contact of menisci with femoral and tibial cartilages. In previous poromechanical modeling, some techniques were used to accelerate the numerical convergence. For instance, in an axisymmetric model of the knee, membrane elements were used on the surface of cartilages and menisci [15]. In a 3D knee model, cartilages were considered as poromechanical, but the menisci were treated as linear elastic solid [24]. The present result indicated the necessity of modeling the menisci as poromechanical.

4.5 *Large vs. Small Deformation Theories*

Many present results in large deformations were qualitatively in agreement with our small deformation results published previously [20,23]. For instance, for the knee in full extension under simple compression, the maximum contact pressure was observed in the medial compartment. The fluid pressure dissipation was much slower in creep than in stress relaxation.

There were some quantitative differences between the results obtained from small and large deformation theories. For instance, the dissipation of fluid pressure was faster in large deformations compared to small deformations. This was probably due to the use of different loading rates in the two scenarios: 300N was applied in one second for small deformations whereas 700N was applied in one second for large deformations. The overall distribution of contact pressure was rather different in small and large deformations, especially at early times (in both creep and stress relaxation): the contact pressure was more evenly distributed across the condyles in small deformations. This discrepancy diminished with creep time. A few reasons may explain the differences. Small sliding contact was used in small deformations whereas finite sliding contact was used for large deformations. Moreover, the initial strains in ligaments were not considered in small deformations, but considered in large deformations. Above all, two

different knees were used in small deformation simulations [22,23] and the large deformation simulations presented herein. The results might be subject-specific.

4.6 *Limitations*

Only one knee was used to perform the present simulations. Another knee was used for small knee compressions. It is not clear on what extent the results are subject-specific. Moreover, the measurements used for model validation were performed on various knees with different ages and gender. Furthermore, the assumptions made in our simulations included simplified fiber orientations, idealized loading and boundary conditions. Tissue mechanical properties may also need further verifications in future studies.

In summary, a fibril-reinforced, viscoelastic poromechanical model in large deformation has been developed to predict the poromechanical response of the knee joint. Cartilages and menisci were modeled as fibril-reinforced porous materials. Quasi-linear viscoelasticity was considered for the collagen network and Neo-Hookean hyperelasticity was used for the non-fibrillar matrix. A user defined FORTRAN subroutine was developed to implement the constitutive law in the commercial software ABAQUS. After numerical tests and experimental validations, the model was used to simulate the creep and stress relaxation of the knee under simple compression. The new formulation and coding are necessary for more realistic numerical approximations since the cartilaginous tissues in the knee are experienced large deformation under physiological loading. The model may be used to clarify the load sharing between articular cartilages and menisci of the knee, which is modulated by fluid pressurization in the cartilaginous tissues. Different load sharing during creep and relaxation indicates a more complicated loading mechanism of the knee joint than that was previously understood.

ACKNOWLEDGEMENTS

We thank Dr. Richard Frayne for his assistance to obtain the MRIs of the knee. The computation was performed at the High Performance Computing Virtual Laboratory, Queen's University in Canada. We appreciate the resource and assistance they have provided.

Conflict of interest: The authors have no conflict of interest to disclose.

Funding: The Canadian Institutes of Health Research; the Natural Sciences and Engineering Research Council of Canada. The first author also received NSERC CREATE and Global Open Doctoral Scholarships.

Ethical approval: E-22593, University of Calgary, for the use of MRI of human subjects.

References

[1] Bendjaballah MZ, Shirazi-Adl A, Zukor DJ. Biomechancis of the human knee joint in compression: reconstruction, mesh generation and finite element analysis. The Knee 1995; 2: 69-79.

[2] Li G, Gil J, Kanamori A, Woo SL. A validated three-dimensional computational model of a human knee joint. Journal of biomechanical engineering 1999; 121(6): 657.

[3] Haut Donahue TL, Hull ML, Rashid MM, Jacobs CR. A finite element model of the human knee joint for the study of tibio-femoral contact. J Biomech Eng 2002; 124: 273-280.

[4] Shirazi R, Shirazi-Adl A, Hurtig M. Role of cartilage collagen fibrils networks in knee joint biomechanics under compression. J Biomech 2008; 41: 3340-3348.

[5] Peña E, Calvo B, Martínez MA, Palanca D, Doblaré M. Finite element analysis of the effect of meniscal tears and meniscectomies on human knee biomechanics. Clin Biomech 2005; 20, 498-507.

[6] Zielinska B, Donahue TL. 3D finite element model of meniscectomy: changes in joint contact behavior. J Biomech Eng 2006; 128: 115-123.

[7] Yang N, Nayeb-Hashemi H, Canavan P K. The combined effect of frontal plane tibiofemoral knee angle and meniscectomy on the cartilage contact stresses and strains. Annals of Biomedical Engineering 2009; 37: 2360-2372.

[8] Shirazi R, Shirazi-Adl A. Analysis of partial meniscectomy and ACL reconstruction in knee joint biomechanics under a combined loading. Clin Biomech 2009; 24, 755-761.

[9] Netravali NA, Koo S, Giori NJ, Andriacchi TP. The effect of kinematic and kinetic changes on meniscal strains during gait. J Biomech Eng 2011; 133(1): 011006.

[10] Peña E, del Palomar A, Calvo B, Martinez M, Doblare M. Computational modelling of diarthrodial joints. Physiological, pathological and pos-surgery simulations. Archives of Computational Methods in Engineering 2007; 14(1): 47-91.

[11] Shirazi R, Shirazi-Adl A. Computational biomechanics of articular cartilage of human knee joint: Effect of osteochondral defects. Journal of Biomechanics 2009; 42(15): 2458-65.

[12] Papaioannou G, Demetropoulos C, King Y. Predicting the effects of knee focal articular surface injury with a patient-specific finite element model. Knee 2010; 17(1): 61-68.

[13] Biot MA. General theory of three-dimensional consolidation. J. Applied Physics 1941; 12: 155-164.

[14] Ateshian GA, Ellis BJ, Weiss JA. Equivalence between short-time biphasic and incompressible elastic material responses. J Biomechanical Eng 2007; 129(3): 405-412.

[15] Wilson W, van Rietbergen B, van Donkelaar CC, Huiskes R. Pathways of load-induced cartilage damage causing cartilage degeneration in the knee after meniscectomy. J Biomech 2003; 36(6): 845-51.

[16] Adeeb SM, Sayed Ahmed EY, Matyas J, Hart DA, Frank CB, Shrive NG. Congruency effects on load bearing in diarthrodial joints. Comput Methods Biomech Biomed Eng 2004; 7(3): 147-57.

[17] Mononen ME, Julkunen P, Töyräs J, Jurvelin JS, Kiviranta I, Korhonen RK. Alterations in structure and properties of collagen network of osteoarthritic and repaired cartilage modify knee joint stresses. Biomech Model Mechanobiol 2011; 10(3): 357-69.

[18] Ateshian GA, Maas S, Weiss JA. Finite element algorithm for frictionless contact of porous permeable media under finite deformation and sliding. J Biomech Eng 2010; 132(6): 061006.

[19] Pérez del Palomar A, Doblaré M. An accurate simulation model of anteriorly displaced TMJ discs with and without reduction. Med. Eng. Phys. 2007; 29: 216-226.

[20] Gu KB, Li LP. A human knee joint model considering fluid pressure and fiber orientation in cartilages and menisci. Med Eng Phys 2011; 33: 497-503.

[21] Li LP, Gu KB. Reconsideration on the use of elastic models to predict the instantaneous load response of the knee joint. Proceedings of the Institution of Mechanical Engineers Part H-Journal of Engineering in Medicine 2011; 225(H9): 888-896.

[22] Kazemi M, Li LP, Savard P, Buschmann MD. Creep behavior of the intact and meniscectomy knee joints. J Mech Behav Biomed Mater 2011; 4(7): 1351-8.

[23] Kazemi M, Li LP, Buschmann MD, Savard P. Partial meniscectomy changes fluid pressurization in articular cartilage in human knees. J Biomech Eng 2012; 134(2): 021001.

[24] Mononen ME, Mikkola MT, Julkunen P, Ojala R, Nieminen MT, Jurvelin JS, Korhonen RK. Effect of superficial collagen patterns and fibrillation of femoral articular cartilage on knee joint mechanics-a 3D finite element analysis. J Biomech 2012; 45(3): 579-87.

[25] Mononen ME, Jurvelin JS, Korhonen RK. Implementation of a gait cycle loading into healthy and meniscectomised knee joint models with fibril-reinforced articular cartilage. Computer Methods in Biomechanics and Biomedical Engineering 2013; DOI: 10.1080/10255842.2013.783575

[26] Fung YC. Stress–strain history relations of soft tissues in simple elongation. In: *Biomechanics: its foundations and objectives*, Englewood Cliffs, NJ: Prentice-Hall, 1972.

[27] Fung YC. *Biomechanics: Mechanical properties of living tissues,* New York: Springer-Verlag, 1993.

[28] Bonet J, Wood RD. *Nonlinear continuum mechanics for finite element analysis,* 2nd ed., Cambridge, UK ; New York: Cambridge University Press, 2008.

[29] Woo SLY, Akeson W H, Jemmott GF. Measurements of nonhomogeneous, directional mechanical properties of articular cartilage in tension. J Biomech 1976; 9: 785-791.

[30] Li LP, Korhonen RK, Iivarinen J, Jurvelin JS, Herzog W. Fluid pressure driven fibril reinforcement in creep and relaxation tests of articular cartilage. Medical engineering & physics 2008; 30(2): 182-189.

[31] Tissakht M, Ahmed AM. Tensile stress-strain characteristics of the human meniscal material. Journal of Biomech 1995; 28(4): 411-422.

[32] Li LP, Buschmann MD, Shirazi-Adl A. Strain rate dependent stiffness of articular cartilage in unconfined compression. J Biomech Eng 2003; 125, 161-168 (Erratum: 125: 566).

[33] Suh JK, Disilvestro MR. Biphasic poroviscoelastic behavior of hydrated biological soft tissue. Journal of Applied Mechanics 1999; 66(2): 528-535.

[34] Li LP, Herzog W. The role of viscoelasticity of collagen fibers in articular cartilage: theory and numerical formulation. Biorheology 2004; 41(3-4): 181-94.

[35] Li LP, Cheung JTM, Herzog W. Three-dimensional fibril-reinforced finite element model of articular cartilage. Medical and Biological Engineering and Computing 2009; 47: 607-615.

[36] Below S, Arnoczky SP, Dodds J, Kooima C, Walter N. The split-line pattern of the distal femur: a consideration in the orientation of autologous cartilage grafts. J Arthroscopic and Related Surgery 2002; 18: 613-617.

[37] Mesfar W, Shirazi-Adl A. Biomechanics of changes in ACL and PCL material properties or prestrains in flexion under muscle force-implications in ligament reconstruction. Comput Methods Biomech Biomed Eng 2006; 9(4): 201-9.

[38] Peña E, Calvo B, Martínez MA, Doblaré M. A three-dimensional finite element analysis of the combined behavior of ligaments and menisci in the healthy human knee joint. J. Biomech 2006; 39: 1686-1701.

[39] Walker PS, Erkman MJ. The role of the menisci in force transmission across the knee. Clin Orthop Relat Res 1975; 109: 184-192.

[40] Kurosawa H, Fukubayashi T, Nakajima H. Load-bearing mode of the knee joint: physical behavior of the knee joint with or without menisci. Clin Orthop Relat Res 1980; 149: 283-90.

[41] Mow VC, Ateshian GA, Spilker RL. Biomechanics of diarthrodial joints: A review of twenty years of progress. J Biomech Eng 1993; 115: 460-467.

[42] Shrive NG, O'connor JJ, Goodfellow JW. Load-bearing in the knee joint. Clinical Orthopaedics and Related Research 1978; 131: 279–287.

[43] Bingham JT, Papannagari R, Van de Velde SK, Gross C., Gill TJ, Felson, DT, Rubash HE, Li G. In vivo cartilage contact deformation in the healthy human tibiofemoral joint. Rheumatology (Oxford) 2008; 47(11): 1622-1627.

[44] Fukubayashi T, Kurosawa H. The contact area and pressure distribution pattern of the knee. A study of normal and osteoarthrotic knee joints. Acta Orthop Scand 1980; 51(6): 871-9.

[45] Brown TD, Shaw D T. In vitro contact stress distribution on the femoral condyles. J Orthop Res 1984; 2(2): 190-9.

[46] Morimoto Y, Ferretti M, Ekdahl M, Smolinski P, Fu FH. Tibiofemoral joint contact area and pressure after single- and double-bundle anterior cruciate ligament reconstruction. Arthroscopy-the Journal of Arthroscopic and Related Surgery 2009; 25(1): 62-69.

[47] Krause WR, Pope MH, Johnson RJ, Wilder DG. Mechanical changes in the knee after meniscectomy. J Bone Joint Surg Am 1976; 58(5): 599-604.

[48] Seedhom B B, Hargreaves DJ. Transmission of the load in the knee joint with special reference to the role of the menisci. Part II: Experimental results, discussion and conclusions. J Engineering in Medicine 1979; 8(4), 220-228.

[49] Inaba HI, Arai MA, Watanabe WW. Influence of the varus-valgus instability on the contact of the femoro-tibial joint. Proceedings of the Institution of Mechanical Engineers, Part H: J Engineering in Medicine 1990; 204(1): 61-64.

[50] Oloyede A, Broom ND. The generalized consolidation of articular cartilage: an investigation of its near-physiological response to static load. Connective tissue research, 1994; 31(1): 75-86.

Appendix A. Numerical Integration of the Fibrillar Stress

Denoting the current time by t_{k+1} and the previous time by t_k, the fibrillar stress (9) at the current time can be expressed as

$$\sigma_x^f(t_{k+1}) = \sigma_x^f(t_k) + \int_{t_k}^{t_{k+1}} G_x(t_{k+1}-\tau)\frac{\partial \sigma_x^e}{\partial \varepsilon_x}\frac{\partial \varepsilon_x}{\partial \tau}d\tau + \int_0^{t_k}\left[G_x(t_{k+1}-\tau)-G_x(t_k-\tau)\right]\frac{\partial \sigma_x^e}{\partial \varepsilon_x}\frac{\partial \varepsilon_x}{\partial \tau}d\tau \qquad \text{(A-1)}$$

Introducing Eq (11), the first integral of (A-1) can be written numerically using a central point formula

$$\int_{t_k}^{t_{k+1}} G_x(t_{k+1}-\tau)\frac{\partial \sigma_x^e}{\partial \varepsilon_x}d\varepsilon_x = G_x(\frac{t_{k+1}-t_k}{2})\left[A_x + B_x\left(\varepsilon_x(t_k)+\varepsilon_x(t_{k+1})\right)\right]\left(\varepsilon_x(t_{k+1})-\varepsilon_x(t_k)\right) \qquad \text{(A-2)}$$

In a numerical procedure, this integral can be calculated after the strain in the previous increment $\varepsilon_x(t_k)$ has been determined.

The calculation of the second integral of (A-1) requires stress and strain data from all previous increments as the limit of this integral is from 0 to t_k. This means that the stress and strain values must be stored at every integration point of each finite element for all time increments. This would require a huge storage of data for our 3D knee modeling. To avoid this problem, the integral must be rewritten in an incremental form depending only on the data from the previous two increments. Introducing Eq (10),

$$\int_0^{t_k}\left[G_x(t_{k+1}-\tau)-G_x(t_k-\tau)\right]\frac{\partial \sigma_x^e}{\partial \varepsilon_x}d\varepsilon_x = \int_0^{t_k}\sum_m g_x^m e^{\frac{\tau-t_k}{\lambda_x^m}}\left(e^{-\frac{\Delta t_{k+1}}{\lambda_x^m}}-1\right)\frac{\partial \sigma_x^e}{\partial \varepsilon_x}d\varepsilon_x = \sum_m\left[g_x^m\left(e^{-\frac{\Delta t_{k+1}}{\lambda_x^m}}-1\right)\zeta_x^m(t_k)\right] \qquad \text{(A-3)}$$

where

$$\zeta_x^m(t_k) = e^{(\frac{-t_k}{\lambda_x^m})} \int_0^{t_k} e^{(\frac{\tau}{\lambda_x^m})} (A_x + 2B_x\varepsilon_x) d\varepsilon_x \tag{A-4}$$

This equation can be further expressed as

$$\zeta_x^m(t_k) = e^{\frac{-t_k}{\lambda_x^m}} \int_0^{t_{k-1}} e^{\frac{\tau}{\lambda_x^m}} (A_x + 2B_x\varepsilon_x) d\varepsilon_x + e^{\frac{-t_k}{\lambda_x^m}} \int_{t_{k-1}}^{t_k} e^{\frac{\tau}{\lambda_x^m}} (A_x + 2B_x\varepsilon_x) d\varepsilon_x \tag{A-5}$$

Noting that $\Delta t_k = t_k - t_{k-1}$ and $\Delta\varepsilon_k = \varepsilon(t_k) - \varepsilon(t_{k-1})$ and using a midpoint formula for the second integral above, Eq. (A-4) takes the numerical form of

$$\zeta_x^m(t_k) = e^{\frac{-\Delta t_k}{\lambda_x^m}} \zeta_x^m(t_{k-1}) + e^{\frac{-\Delta t_k}{2\lambda_x^m}} \left[A_x + B_x \left(\varepsilon_x(t_{k-1}) + \varepsilon_x(t_k) \right) \right] \Delta\varepsilon_k \tag{A-6}$$

Therefore, the fibrillar stress takes the final numerical form of

$$\sigma_i^f(t_{k+1}) = \sigma_i^f(t_k) + G_i(\frac{\Delta t_{k+1}}{2}) \times \left[A_i + B_i \left(\varepsilon_i(t_k) + \varepsilon_i(t_{k+1}) \right) \right] \left(\varepsilon_i(t_{k+1}) - \varepsilon_i(t_k) \right) + \sum_m g_i^m \left(e^{-\frac{\Delta t_{k+1}}{\lambda_i^m}} - 1 \right) \zeta_i^m(t_k)$$

$$(i = x, y, z) \tag{A-7}$$

Table 1 Geometrical parameters and material properties of the model used to fit the experimental stress relaxation and creep tests of a tissue explant. k is the hydraulic permeability of the tissue defined by Darcy's law.

<table>
<tr><td rowspan="2">Disk dimension</td><td>Fibrillar collagen network

Eq. (11)</td><td>Non-fibrillar porous matrix

Eq. (5)</td></tr>
<tr><td rowspan="2">A = 2.0 MPa

B = 767.1 MPa</td><td>C_{10} = 0.115 MPa

D_1 = 4.0 MPa^{-1}

k = 0.001 mm^4/Ns</td></tr>
<tr><td>Diameter: 3.02 mm

Thickness:

1.66 mm</td><td colspan="2">Reduced relaxation coefficients, Eq. (10):

g^1=0.6, λ^1=10, g^2=0.7, λ^2=100, g^3=0.2, λ^3=1000</td></tr>
</table>

Table 2. Changes in the maximum contact pressure in a step-by-step mesh sensitivity study, as compared to the pressure obtained from the reference mesh. Fluid pressure was not considered in the sensitivity study. The reference mesh was used for the full simulations of the knee joint with fluid pressures.

Mesh	Number of elements in each tissue			Change in maximum contact pressure (%)
	Femoral cartilage	Menisci	Tibial cartilages	
Reference	7476	4144	4638	N/A
Step 1	29904	4144	4638	1.9
Step 2	29904	33152	4638	5.4
Step 3	29904	33152	37104	8.1

Table 3. Material properties of the collagen network and the non-fibrillar solid matrix of all soft tissues

	Fibrillar collagen network Eq. (18)				Non-fibrillar matrix Eq. (5)	
	Primary fiber direction (x), (MPa)		Perpendicular directions (y, z), (MPa)		C_{10} (MPa)	D_1 (MPa^{-1})
	A	B	A	B		
Femoral cartilage	1.376	367.14	0.413	110.14	0.176	0.96
Tibial cartilages	0.918	229.46	0.918	229.46	0.183	1.68
Menisci	12.84	0.0	2.295	0.0	0.880	0.192
Ligaments	46.47	1118.6	0.0	0.0	0.385	1.2
Reduced relaxation coefficients, in Eq. (10), for all tissues in x, y and z directions: g^1=0.87, λ^1=10, g^2=0.036, λ^2=100, g^3=0.273, λ^3=1000						
Hydraulic permeability for cartilaginous tissues (Darcy's law): k_x=0.002 mm^4/Ns, k_y=0.001, k_z=0.001						

1

FIGURE CAPTIONS

Figure 1. Comparison of the computational with experimental results on cartilage explants. (a) Stress relaxation; and (b) creep. The same material parameters were used to fit the relaxation and creep tests simultaneously. The material and geometrical parameters used in the computations were presented in Table 1.

Figure 2. The knee joint geometry reconstructed from magnetic resonance images (a) and meshed with finite elements (b). The model includes femur, tibia, fibula, articular cartilages, menisci and ligaments. It is from the right knee of a 27-year Caucasian male with no leg injury history.

Figure 3. Contact pressure distributions on the articular surface of femoral cartilage for creep at a) 1s, and b) 100s. Inferior view; medial condyle on the right.

Figure 4. Maximum contact pressure in femoral cartilage and menisci as a function of time. (a) creep; and (b) stress relaxation.

Figure 5. Knee compressive displacement as a function of applied force, numerical prediction versus experimental measurements. The experimental data were taken from the literature [39,40,42]. Maximum applied load in the present study was 700N (force control).

Figure 6. Normal strain in the surface layer of tibial cartilages in the direction of knee compression under creep loading at (a) 1s, and (b) 100s. Superior view; medial side on the right.

Figure 7. Maximum fluid pressure in the femoral cartilage as a function of time for (a) creep; and (b) stress relaxation. The fluid pressure was obtained from the centroids of elements which were approximately at 3/8 depth from the articular surface. For the case of viscoelastic fibers, the stiffness of the fibrillar network decreased with time as indicated by the reduced relaxation

function (Eq. 10); for the case of elastic fibers, the stiffness was taken to be the initial stiffness of the fibrillar network with no reduction in time.

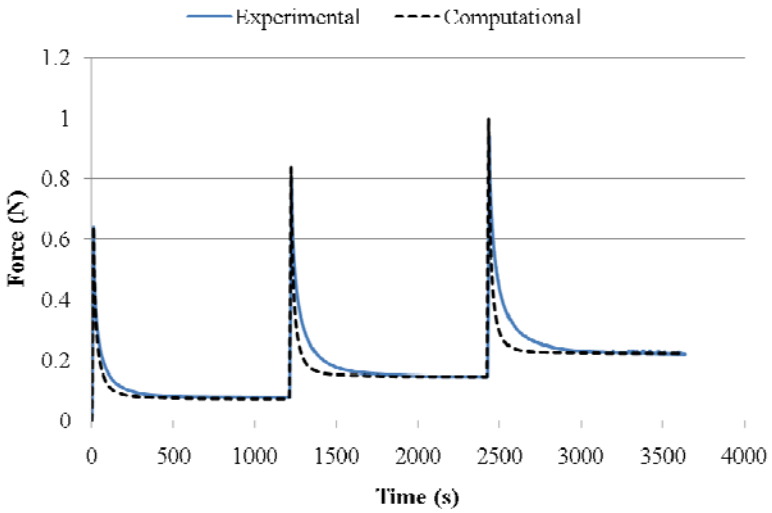
Experimental
Computational
Force (N)
Time (s)
0
0.2
0.4
0.6
0.8
1
1.2
0
500
1000
1500
2000
2500
3000
3500
4000

a)

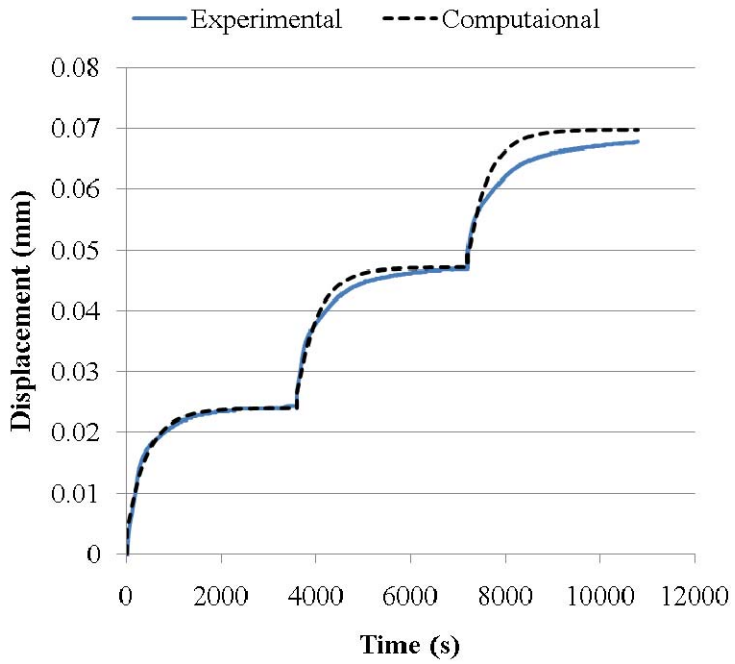
Experimental
Computaional
Displacement (mm)
Time (s)
0
0.01
0.02
0.03
0.04
0.05
0.06
0.07
0.08
0
2000
4000
6000
8000
10000
12000

b)

Fig. 1

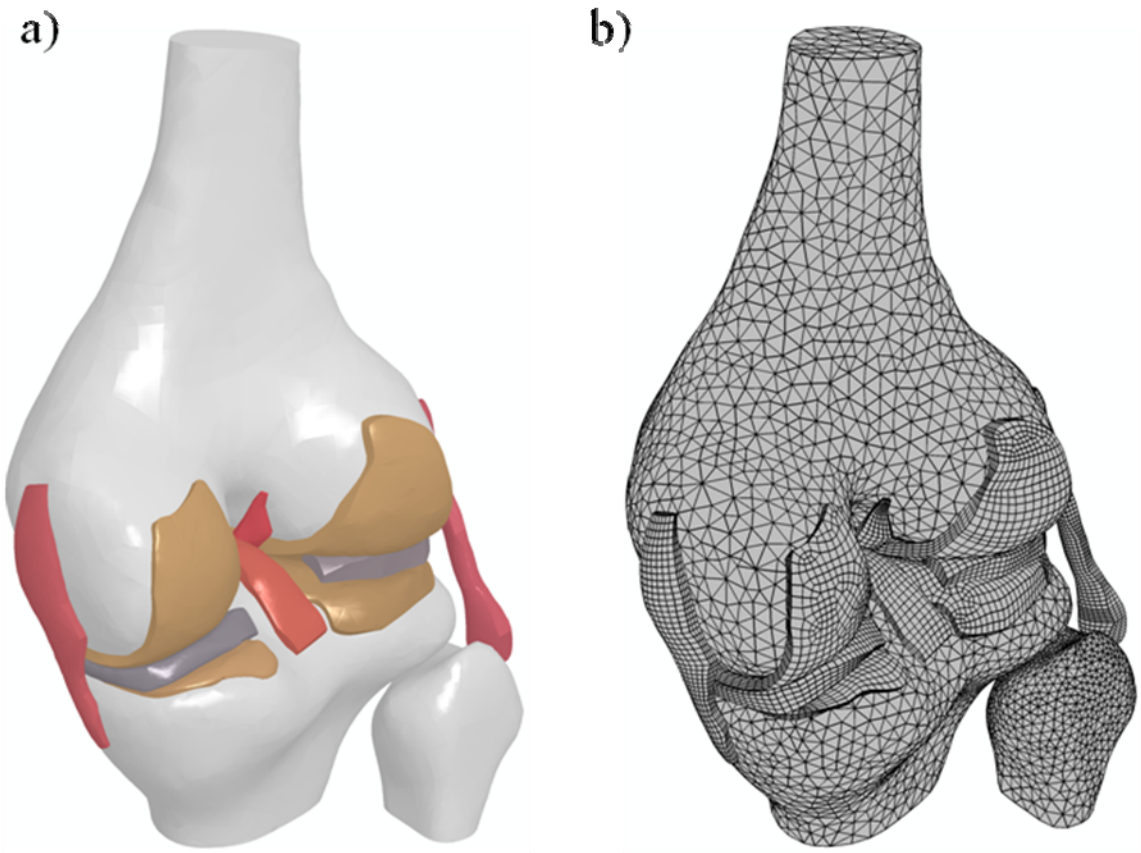

Fig. 2

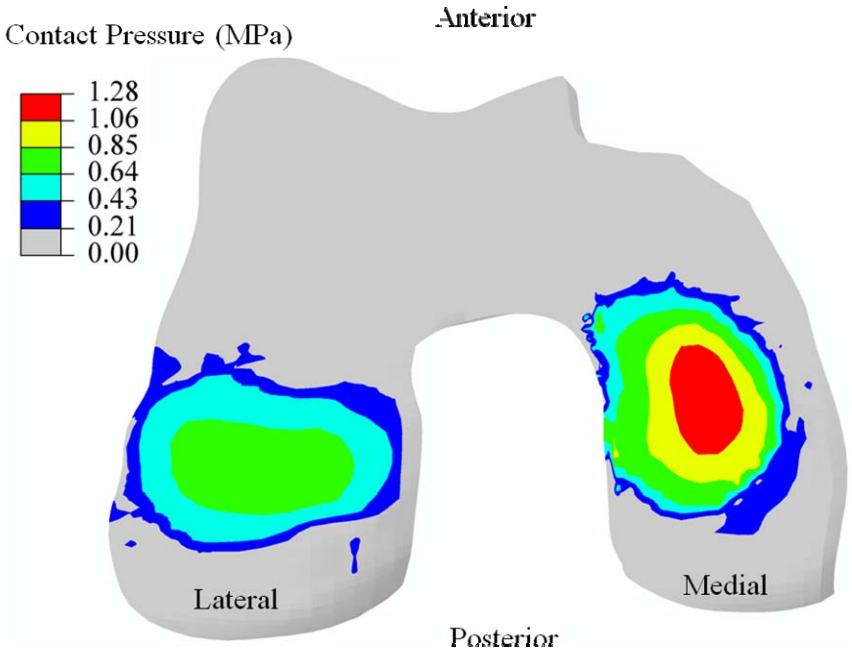
Contact Pressure (MPa)
1.28
1.06
0.85
0.64
0.43
0.21
0.00
Anterior
Lateral
Medial
Posterior

a)

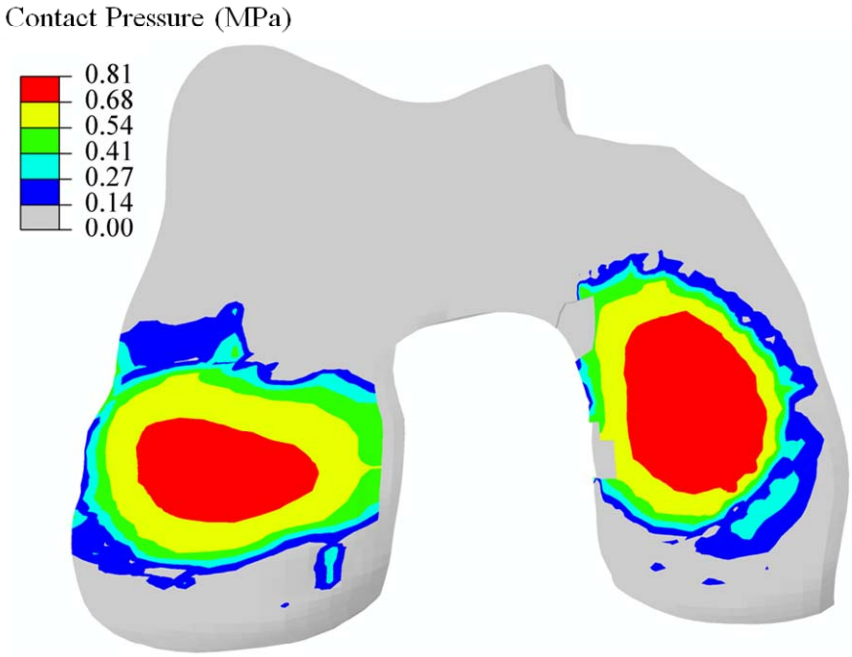
Contact Pressure (MPa)
0.81
0.68
0.54
0.41
0.27
0.14
0.00

b)

Fig. 3

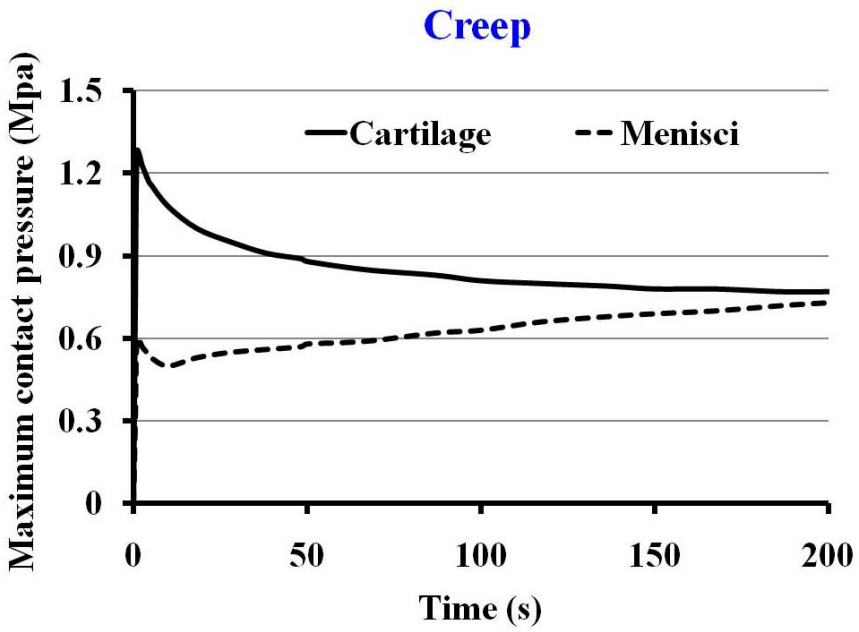
Creep
Maximum contact pressure (Mpa)
1.5
1.2
0.9
0.6
0.3
0
Cartilage
Menisci
0
50
100
150
200
Time (s)

a)

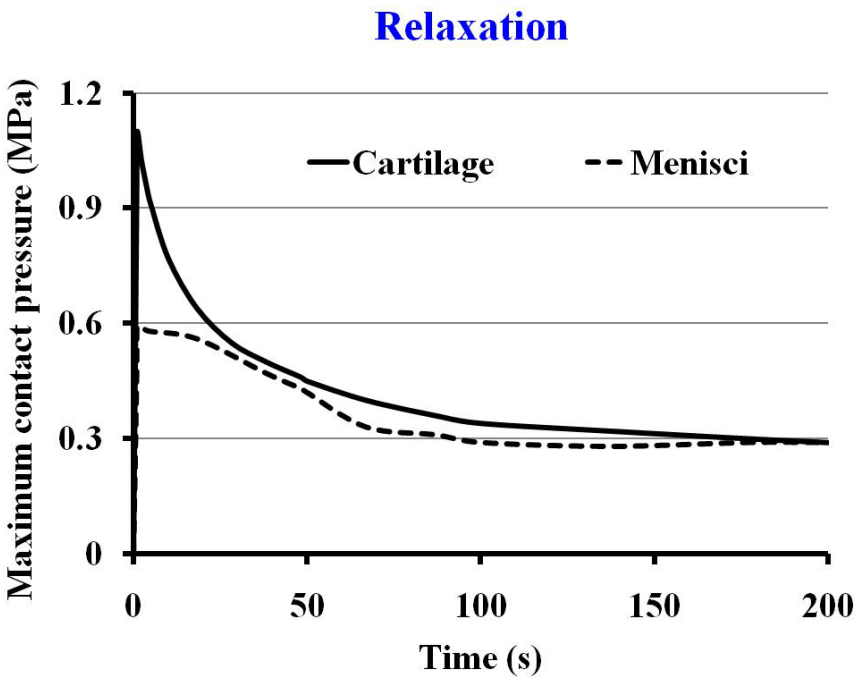
Relaxation
Maximum contact pressure (MPa)
1.2
0.9
0.6
0.3
0
Cartilage
Menisci
0
50
100
150
200
Time (s)

b)

Fig. 4

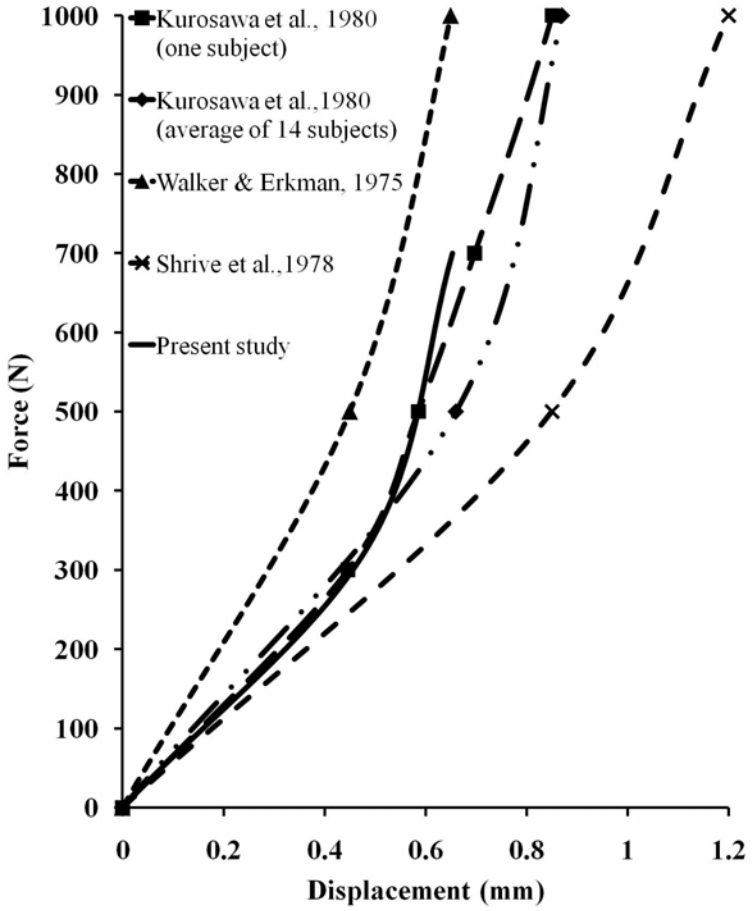
Kurosawa et al., 1980
(one subject)
Kurosawa et al.,1980
(average of 14 subjects)
Walker & Erkman, 1975
Shrive et al.,1978
Present study
Force (N)
Displacement (mm)
0
100
200
300
400
500
600
700
800
900
1000
0
0.2
0.4
0.6
0.8
1
1.2

Fig. 5

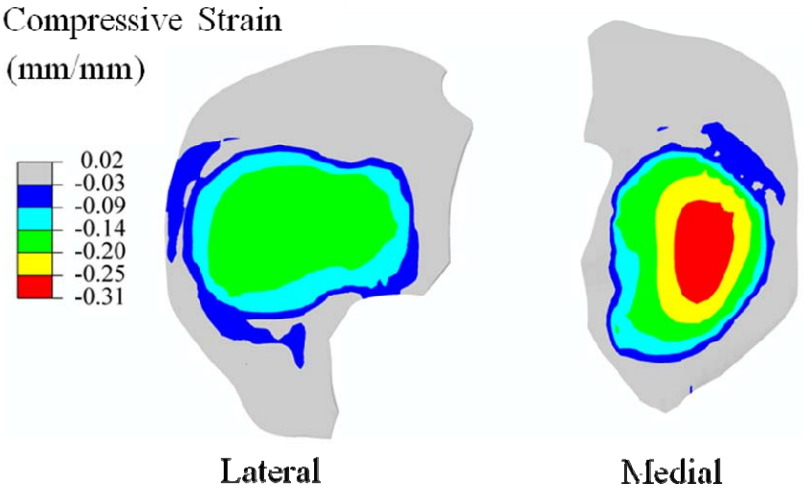
Compressive Strain
(mm/mm)
0.02
-0.03
-0.09
-0.14
-0.20
-0.25
-0.31
Lateral
Medial

a)

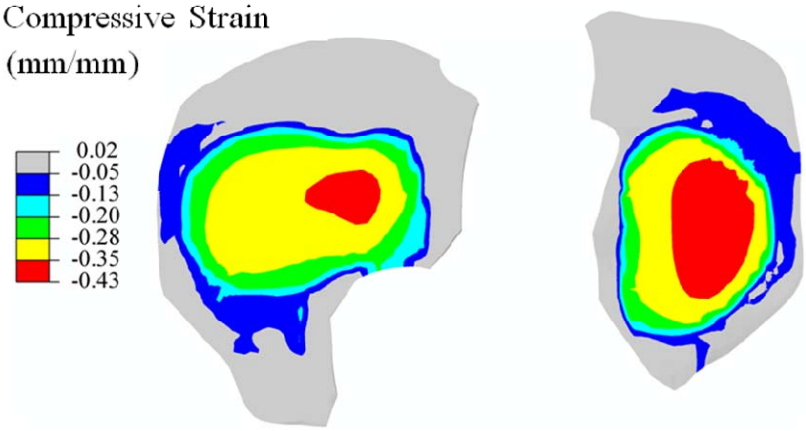
Compressive Strain
(mm/mm)
0.02
-0.05
-0.13
-0.20
-0.28
-0.35
-0.43

b)

Fig. 6

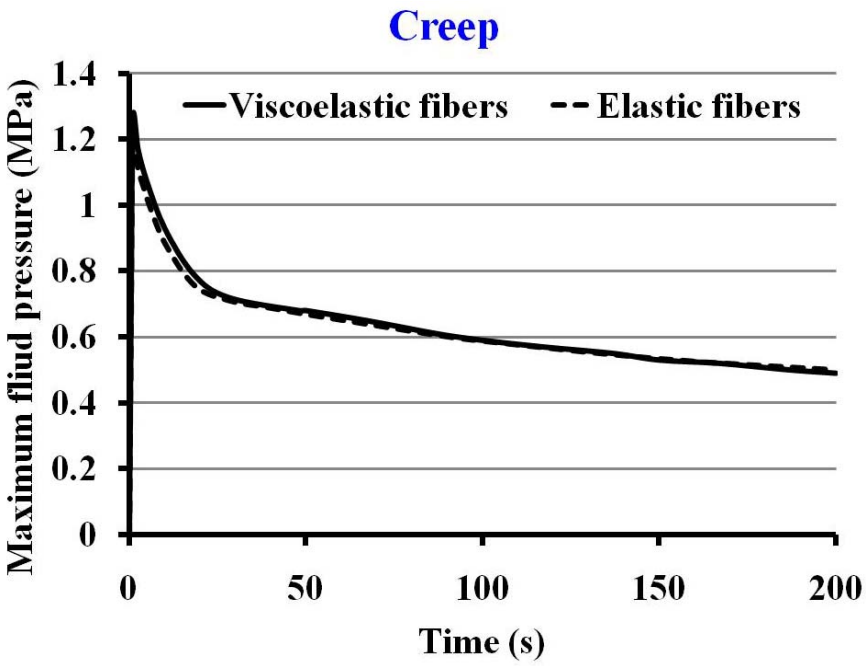
Creep
Viscoelastic fibers
Elastic fibers
Maximum fliud pressure (MPa)
1.4
1.2
1
0.8
0.6
0.4
0.2
0
0
50
100
150
200
Time (s)

a)

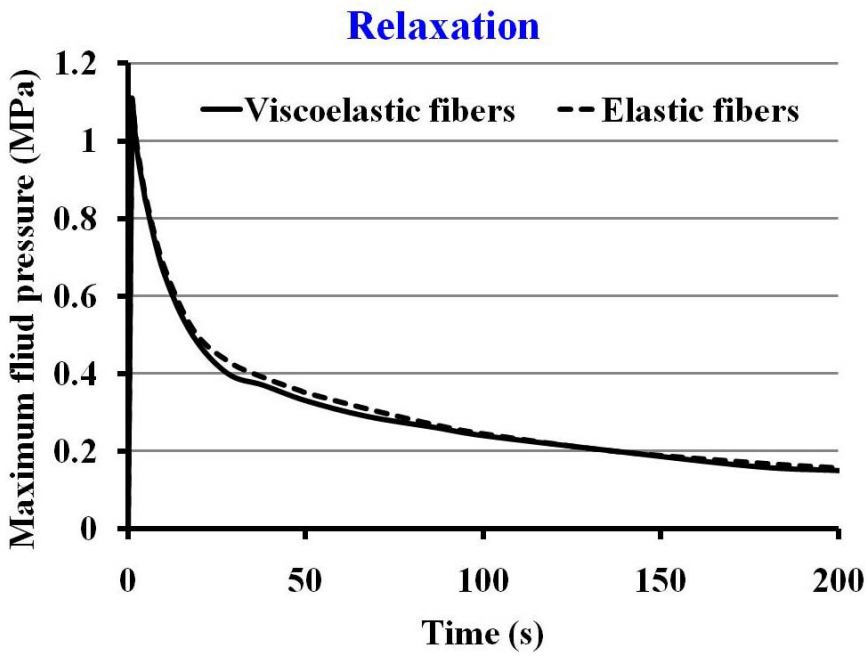
Relaxation
Viscoelastic fibers
Elastic fibers
Maximum fliud pressure (MPa)
1.2
1
0.8
0.6
0.4
0.2
0
0
50
100
150
200
Time (s)

b)

Fig. 7